



APPLIED SCIENCES AND ENGINEERING

Direct quantification of ion composition and mobility in organic mixed ionic-electronic conductors

Ruiheng Wu¹, Xudong Ji^{2*}, Qing Ma³, Bryan D. Paulsen², Joshua Tropp², Jonathan Rivnay^{2,4*}

Ion transport in organic mixed ionic-electronic conductors (OMIECs) is crucial due to its direct impact on device response time and operating mechanisms but is often assessed indirectly or necessitates extra assumptions. Operando x-ray fluorescence (XRF) is a powerful, direct probe for elemental characterization of bulk OMIECs and was used to directly quantify ion composition and mobility in a model OMIEC, poly(3,4-ethylenedioxythiophene)-poly(styrene sulfonate) (PEDOT:PSS), during device operation. The first cycle revealed slow electro wetting and cation-proton exchange. Subsequent cycles showed rapid response with minor cation fluctuation (~5%). Comparison with optical-tracked electrochromic fronts revealed mesoscale structure-dependent proton transport. The calculated effective ion mobility demonstrated thickness-dependent behavior, emphasizing an interfacial ion transport pathway with a higher mobile ion density. The decoupling of interfacial effects on bulk ion mobility and the decoupling of cation and proton migration elucidate ion transport in conventional and emerging OMIEC-based devices and has broader implications for other ionic conductors writ large.

INTRODUCTION

Organic mixed ionic-electronic conductors (OMIECs) are materials that transport both ions and electrons (1), making them highly versatile for a wide range of applications such as energy storage (2), neuro-morphics (3, 4), and bioelectronics (5–9). To guide the development of energy-efficient, high-performance sensors and circuits for these applications, understanding the fundamental operating mechanisms of OMIEC-based devices, in particular the complex mixed ion/electron transport and coupling within OMIECs, is critical. Electronic or coupled electronic/ionic properties such as electronic mobility μ and volumetric capacitance C^* and the related material figure of merit μC^* (10, 11) have been extensively investigated (1, 12, 13). However, directly determining ion composition and mobility in device-relevant conditions is challenging due to the presence of an electrolyte background and the relatively limited availability of operando elemental analysis techniques.

Efforts have been made in previous studies to quantify the ion composition in OMIECs (14–16), although most of these works are based on indirect approaches such as electrochemical quartz crystal microbalance (14, 15). More recently, operando nuclear magnetic resonance (NMR) has been used as a direct approach to study the ion composition in poly(3,4-ethylenedioxythiophene)-poly(styrene sulfonate) (PEDOT:PSS) (16), while the generalizability of this study has been limited owing to the usage of millimeter-thick films and nonstandard electrolytes. This technique is also unable to effectively distinguish between free cations in the film and those in the electrolyte due to the presence of residual electrolyte within the NMR coil.

Similarly, research on ion transport in OMIECs has predominantly relied on indirect evidence. The signals detected by microprobe-based techniques, such as scanning electrochemical microscopy (SECM) (17) and electrochemical strain microscopy (ESM) (18), might inaccurately depict the behavior of the targeted ionic dopants owing to

the solvent-related effects. SECM requires the presence of electroactive species to generate measurable currents, making it unsuitable for nonelectroactive cations (e.g., Na^+ , Rb^+ , and Ca^{2+}); while ESM conflates the ion transport with water transport, as the observed swelling is related to the hydration shell (15). Optical methods like the electrochromic moving front (Fig. 1A) have also been applied to indirectly track ion transport in OMIECs and derive information on the rate of ion transport through the polymer matrix (19–21). However, these indirect optical studies involve assumptions, such as single ion transport within the polymer and that the progressing electrochromic moving front is rate limited by ion transport instead of hole transport (22). A recent report suggests that on longer timescales, ion transport is primarily driven by the internal electrostatic fields within OMIECs, generated by hole displacement currents (23). These assumptions limit the accuracy and reliability of previously reported moving front experiments, highlighting the need for direct measurement of both ion composition and mobility in OMIECs.

Different geometries in OMIEC-based devices introduce additional complexity as the direction of ion transport with respect to film texture and interface can be variable. Because of their processability, chemical tunability, and compatibility with aqueous electrolytes, OMIECs are widely used in organic electrochemical transistors (OECTs) (10). Conventional OECTs (cOECTs) use a planar source-drain electrode structure (Fig. 1B), where the dominant ion transport occurs vertically between the thin film and the electrolyte, while electronic transport occurs laterally within the OMIEC channel (1). Vertical ion migration is limited by the ion mobility in bulk OMIECs. Recently, a new vertical OECT (vOECT) architecture has been reported (Fig. 1C) (24), featuring a vertically scalable structure and narrow channel lengths controlled by the film thickness, which effectively improve device integration density and sensitivity. In contrast to cOECTs, vOECTs involve lateral ion transport within the encapsulated OMIEC channel, highlighting the interfacial ion transport; despite the anticipated longer ion migration distances required for complete channel doping in vOECTs, their response times have been observed to be comparable to those of cOECTs in operation (24). To further elucidate ion transport in OECTs with different geometries, it is important to decouple ion transport within the bulk from transport at the interfaces.

¹Department of Chemistry, Northwestern University, Evanston, IL 60208, USA. ²Department of Biomedical Engineering, Northwestern University, Evanston, IL 60208, USA. ³DND-CAT, Synchrotron Research Center, Northwestern University, Evanston, IL 60208, USA. ⁴Department of Material Science and Engineering, Northwestern University, Evanston, IL 60611, USA.

*Corresponding author. Email: xudong.ji@northwestern.edu (X.J.); jrivnay@northwestern.edu (J.R.)

Copyright © 2024 the Authors, some rights reserved; exclusive licensee American Association for the Advancement of Science. No claim to original U.S. Government Works. Distributed under a Creative Commons Attribution NonCommercial License 4.0 (CC BY-NC).

Downloaded from https://www.science.org at DOE Office of Science on October 29, 2024

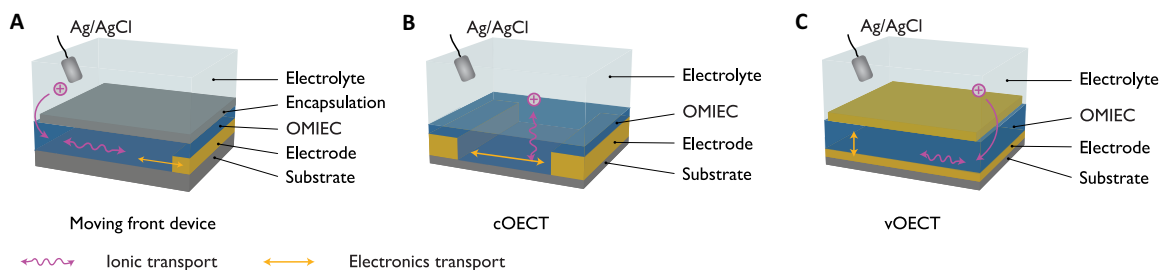


Fig. 1. Different device geometries. Ion and electron transport in (A) moving front device, (B) cOECT, and (C) vOECT. The cartoons are adapted from (1).

In this study, we introduce a direct approach to quantify ion composition and mobility in OMIECs using operando x-ray fluorescence (XRF). Ex situ XRF has been used to quantify ion composition in OMIECs under different doping states, but potential errors arise due to sample postwashing used to remove residual electrolyte and from sample-to-sample variability (25). In contrast, operando XRF measurements separate the incident x-ray pathway from the electrolyte, allowing for real-time measurement of ion composition during electrochemical cycling. This noninvasive technique directly tracks ion mobility from the corresponding elemental peak changes, eliminating the need for additional assumptions on indirect evidence.

This study focuses on a model OMIEC system, PEDOT:PSS, prepared from an aqueous dispersion with ethylene glycol (EG) as a cosolvent additive. This system is known for its high electronic conductivity, facile processability, commercial availability, and wide applicability and has been extensively studied (20, 25–27). The addition of EG to PEDOT:PSS enhances its electronic conductivity by forming locally ordered mesoscale domains (20), thus overcoming hole transport limitations (22, 28). The degree of phase separation and purity can be tuned by adjusting the EG content (20), making it an excellent system for investigating ionic composition and transport during operation. The combination of elemental analysis with thorough thickness-dependent studies reported here have upended the previously understood relationship between bulk cation mobility, EG content, and film morphology (20), revealing that interfacial effects had previously masked bulk cation transport behavior. Specifically, operando XRF has revealed that proton transport cannot be disregarded in low EG content samples with reduced phase purity, and anion transport cannot be disregarded in the interfacial dominated thin-film limit, especially in vOECT architecture, such that Donnan exclusion (25) cannot always be presumed.

Our findings offer valuable insights into ion transport in OMIECs and the behavior of related devices and circuits. This direct approach for quantifying ion composition and mobility will serve as a basis for molecular design, materials processing, and charge/ion migration modeling, with implications for device performance. Not solely confined to OMIECs, this method can also be applied to investigate complex ion transport mechanisms in various mixed conductors, spanning fields including batteries and solar cells.

RESULTS

To directly measure ion composition during electrochemical cycling of films, we developed an operando XRF setup that featured a 3D-printed cell, an Ag/AgCl reference/counter electrode, and a fixed PEDOT:PSS-coated glass slide. We note that the cross-linker (3-glycidylxypropyl)-trimethoxysilane (GOPS) was excluded in the

film formulation to be in line with previous electrochromic moving front study (20). We anticipate a slower moving front and lower ion concentration in the PEDOT:PSS films with GOPS. A parylene layer was introduced between the PEDOT:PSS and the glass substrate to prevent material delamination. The coated glass slide was further covered by a hydrophobic encapsulation layer (SU-8) on top (Fig. 2A and XRF background in fig. S1). Appropriate thickness of encapsulation layer was chosen for accurate determination of ionic composition and mobility (see the “Operando XRF cell description” section in Materials and Methods). A $23,000 \mu\text{m} \times 20 \mu\text{m}$ opening was patterned on the lower end of the encapsulation layer to expose the sealed OMIEC film to the aqueous electrolyte. An external voltage was applied to induce ion migration laterally (upward) from the opening, to counterbalance the electronic charges removed/injected. As a result, an electrochromic front was observed to move upward through the dedoped polymer. Notably, we used heavier ions (Rb^+ and Br^-) as substitutes for Na^+/K^+ and Cl^- , building on prior studies (25, 29), due to their strong fluorescence that is readily monitored in ambient within the electrochromic front. To further investigate the kinetics of composition modulation, across the measurement, the incident x-ray beam was held at fixed distances from the opening and the changes of corresponding elemental fluorescence peak intensity were measured with the XRF detector. The collected XRF spectra (Fig. 2B and fig. S2) were analyzed to calculate the actual elemental ratios of Rb (transported from the RbBr electrolyte) and S (inherent from thiophene and/or sulfonate) in the PEDOT:PSS films (Fig. 2C) based on calibration curves (detail and error analysis in section S1 and figs. S3 to S5). The As fluorescence peaks (at 10.5 and 11.7 keV) from the glass background were used for spectrum normalization.

Electrowetting of dry OMIEC film

During the first dedoping process (-1 V versus Ag/AgCl in 0.1 M RbBr), PEDOT:PSS films experienced substantial proton-cation exchange driven by external dedoping potential. This exchange is expected to take place during the initial operation in top-encapsulated vOECTs, differing from passive ion exchange in nonencapsulated cOECTs exposed to an aqueous electrolyte. Balancing film homogeneity and signal-to-noise ratio, drop-casted 20% EG mixed PEDOT:PSS (20% EG-PEDOT:PSS) films were first used for quantitative ion composition analysis. Under a dedoping voltage of -1 V versus Ag/AgCl, the ion moving front advanced by $\sim 7 \text{ mm}$ in 10 hours, spatially below the position the electrochromic equilibrium reached (fig. S6 and Fig. 2, D and E). In the region showing a color change, only a gradual increase in the Rb fluorescence was observed (owing to the Rb^+ cation), but no Br fluorescence was observed (from the Br^- anion) (Fig. 2C), confirming the Donnan exclusion reported in ex situ characterization of PEDOT:PSS/EG

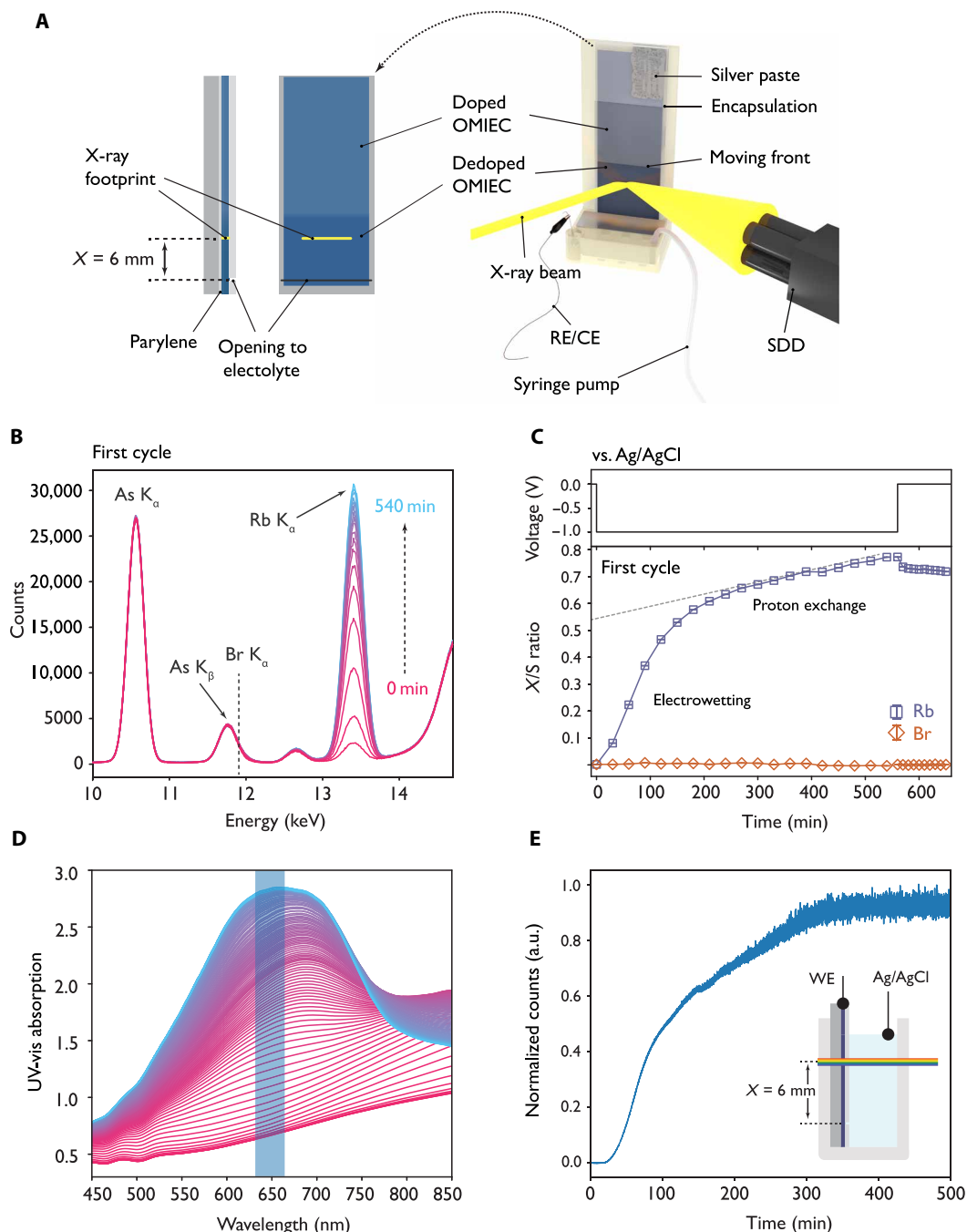


Fig. 2. Electrowetting and proton-cation exchange in the first electrochemical cycle. (A) Side, front, and 3D view of operando XRF setup. (B) XRF spectra for drop-casted 20% EG-PEDOT:PSS in the first dedoping (-1 V versus Ag/AgCl) process. The distance between the opening gap and x-ray beam footprint X is 6 mm. (C) Ion transport curve during the first dedoping process at $X = 6$ mm, with Rb in violet squares and Br in brown diamonds. (D) UV-vis absorbance data of a 20% EG-PEDOT:PSS film as the dedoping electrowetting front moves past the optical fiber. The distance between the opening gap and light spot X is 6 mm. (E) The neutral peak absorbance (at 650 nm) as a function of dedoping time at $X = 6$ mm. In (B) and (D), the curve changing from red to blue represents the gradual increase in dedoping time. a.u., arbitrary units.

films (25). At the end of the dedoping process, the ratio of Rb to S in the bulk phase was 0.7 to 0.8 (error analysis in the Supplementary Materials). Assuming a sulfonate S (S on PSS⁻) to total S ratio of 0.75 [fig. S7; 0.71 in (30)], most of the fixed anions on PSS polyelectrolyte in the dedoped bulk film were balanced by the external cations, which exchanged protons in the original pristine film.

The Rb⁺ cation accumulation in the first dedoping process can be divided into two stages (Fig. 2C): A faster ion transport equilibrated in the first 250 min, followed by a subsequent slower quasi-linear Rb⁺ accumulation. By extrapolating this tail, a Rb/S ratio of 0.52 is obtained from the intercept, representing the equilibrated Rb⁺ concentration of the first stage. This number matches our previous

report through ex situ XRF in thin PEDOT:PSS films (25) and bounded cation concentration measured by operando NMR in millimeter-thick films (16). The equilibrated Rb/S ratio (0.52) is notably lower than the sulfonate content (0.75 of the total S), implying a substantial minority proton population still trapped in the film after the first stage of proton-cation exchange. At the end of the first stage, the spectroscopic signature of neutral absorption (650 nm) stabilized (Fig. 2E), which implies a constant hole density in the second stage. Thus, the further Rb⁺ concentration increase in the second stage does not reflect a further increase in hole concentration (i.e., doping) but instead indicates additional cation-proton exchange, which will be discussed later. Compositionally, in this first stage, external Rb⁺ cations compensate for the holes leaving the film and replace the weakly trapped protons inside the film.

The fast initial stage in these samples reflects the ion moving front caused by the electrowetting. Electrowetting occurs due to the interplay of surface energy reduction and the Maxwell stress generated by the electric field near the dry-wet interface (thus attracting free charges and polarized dipoles), resulting in the decrease of contact angle and a hydrophilic interface (31). The speed of the electrowetting process extracted from the samples with a thick encapsulation layer (25 μm) is 20 μm/min (fig. S8) and 37 μm/min (fig. S9) for drop-casted 5% EG- and 20% EG-PEDOT:PSS, respectively. OMIECs undergo film swelling during the wetting process which is, in part, mechanically countered by the encapsulation layer. Thus, the electrowetting speed depends on various complex factors, including the thickness and mechanical properties of both the encapsulation layer and the OMIEC film, as well as the device geometry. Specifically, the top gold electrode and polymeric encapsulation layer in vOECT is expected to cause a potential slowdown in electrowetting speed during the initial electrochemical cycles. Consequently, vOECTs may require an extended precycling period to effectively use the entire channel area compared to cOECTs.

The subsequent linear increase of cations is attributed to an electronic field induced ion exchange between the Rb⁺ and the residual strongly trapped protons in the OMIEC film. This exchange process does not occur effectively when the film is passively exposed to salt or undergoes short-term electrochemical cycling without an extended “break-in.” EG-mixed PEDOT:PSS consists of purified PEDOT-rich cores and PSS-rich matrices. The PEDOT-rich cores function as electronic conducting pathways, while the PSS-rich matrices serve as ion transport pathways. Initially, external ions are expected to exchange the protons in the more hydrophilic PSS-rich matrices as they traverse through this matrix. Continuing to apply reductive voltages leads to the gradual displacement by Rb⁺ of deeply trapped protons, which may be residing in the less hydrophilic PEDOT-rich domains. Together, these data indicate the presence of two populations of protons in PEDOT:PSS and underscore the interdependence of weakly trapped proton exchange and hole transport, especially in the lateral ion transport scenario.

Direct measurement of ion composition and mobility in electrochemical cycling

After the first dedoping process (stepping to −1 V versus Ag/AgCl), the modulation of ion composition in 20% EG-PEDOT:PSS films decreased in the following electrochemical cycles. The first redoping (stepping to 0 V versus Ag/AgCl; fig. S10) resulted in approximately 7% of Rb⁺ cations migrating out the film. Subsequently, we conducted multiple electrochemical cycles (between dedoped and doped states) on the sample and analyzed the ionic composition in different doped

states (Fig. 3, A and B). When the polymer is fully dedoped (−0.6 or −1 V versus Ag/AgCl, above the reductive onset of 20% EG-PEDOT:PSS), the modulation of the Rb⁺ concentration between dedoped and doped states remained stabilized (~5%; Fig. 3B). The decreased Rb⁺ concentration modulation from the initial redoping process (Fig. 3C) indicates some ion trapping after multiple electrochemical cycles. Nonetheless, the compositional findings emphasize an internal ion reservoir of mobile cations and fixed PSS anions (32), possibly distributed heterogeneously in a mesoscale morphology within PEDOT:PSS (32, 33).

To obtain the ion mobility in sufficiently swelled OMIECs, we performed several electrochemical cycles on the samples with thick encapsulation layers (detail in Materials and Methods). This is akin to the precycling or break-in often performed, especially in previous optical moving front experiments (19–22). After five to six cycles, the response curves for the ion concentration at the same position stabilized (fig. S11). The modulation of cations in different samples under the doped and dedoped states was in the range of 5 to 10%. A sigmoid fit to these corresponding curves gave the time required for Rb⁺ to migrate a specific distance (Fig. 3D), thus obtaining the ion mobility through the model developed by Stavrinidou *et al.* (19). Specifically, this method gave a Rb⁺ mobility of $3.8 \times 10^{-3} \text{ cm}^2 \text{ s}^{-1} \text{ V}^{-1}$ for drop-casted 20% EG-PEDOT:PSS. The reliability of this model was also supported by the kinetic curves when the samples were dedoping under −0.6 V versus Ag/AgCl (fig. S12). Notably, this model did not capture the kinetics of the redoping process (0 V versus Ag/AgCl). Instead, we observed a spontaneous ion outflux following exponential decay kinetics (fig. S13 and section S2).

Proton transport across mesoscale domain boundaries

The moving front was also measured optically immediately after the operando XRF experiments to compare the electrochromic and elemental fronts in the same sample. Influenced by the EG content during the sample preparation process, the progression of these two moving fronts (ionic and electrochromic) matched in 20% EG-PEDOT:PSS but diverged in 5% EG-PEDOT:PSS. The evolution of the electrochromic moving front is shown in Fig. 4A and fig. S14B, for drop-casted 20% EG- and 5% EG-PEDOT:PSS, respectively. The propagation rate of the electrochromic moving front can be extracted from the kinetic curves measured at different distances from the encapsulation opening. For 20% EG-PEDOT:PSS, the cation mobilities from both electrochromic-based measurements (19, 20) and operando XRF were comparable (Fig. 4B). However, for 5% EG-PEDOT:PSS, the cation mobility obtained by XRF measurements was lower than that obtained from optical methods (Fig. 4B). To assess the reliability of the optical moving front on drop-casted samples, we conducted optical measurements on drop-casted EG-PEDOT:PSS samples with different EG content. In line with the report by Rivnay *et al.* (20) for spin-coated samples, these drop-casted samples also exhibit a decelerated optical moving front with increased EG content (figs. S14 and S15). The disparity between the optical and XRF moving fronts in low EG content PEDOT:PSS film indicated the presence of other ions in the system that affected the electrochromic moving front.

Since no mobile anions were present in drop-casted 5% EG-PEDOT:PSS, we hypothesized that the inconsistency between the optical moving front and the Rb⁺ moving front arose from proton transport. To simulate the observed faster optical moving front in the 5% EG-PEDOT:PSS, we conducted optical measurements on drop-casted 20% EG-PEDOT:PSS films after cycled and stabilized

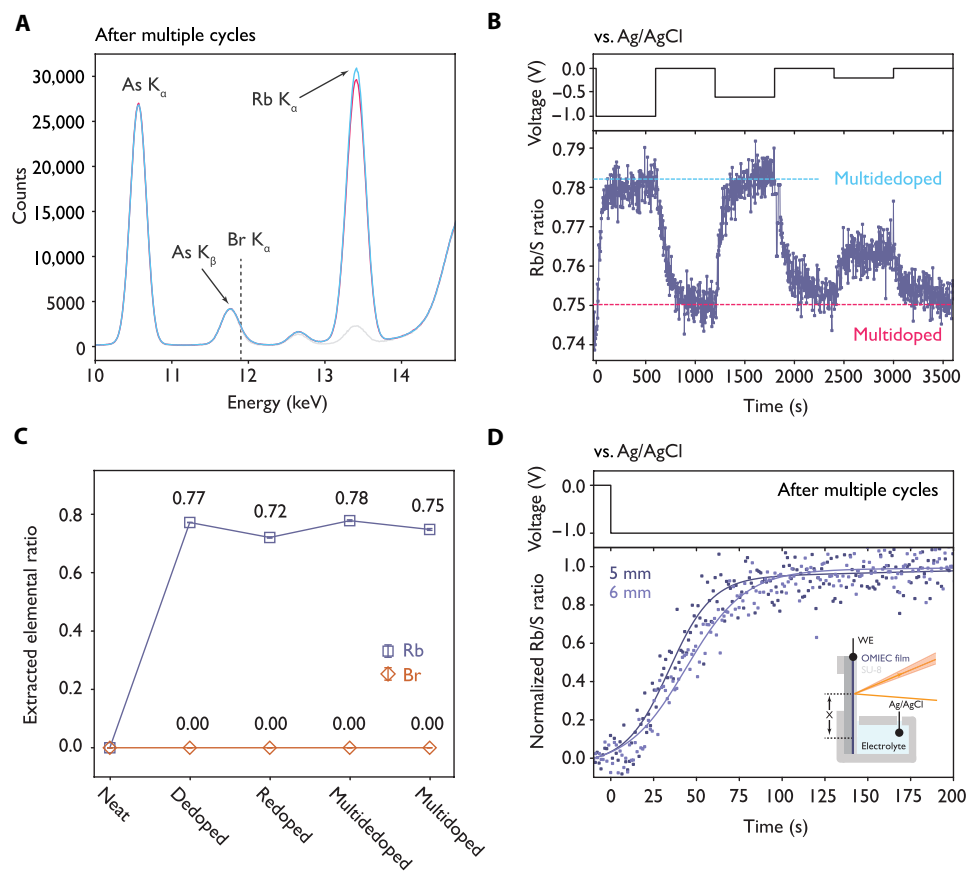


Fig. 3. Quantifying ion composition and transport kinetics in following electrochemical cycling. (A) XRF spectra for drop-casted 20% EG-PEDOT:PSS in dedoped (blue) and doped state (magenta) after multiple electrochemical cycles; the baseline is plotted in gray. (B) Rb^+ transport curve during the later electrochemical cycling process (dedoped at -1 , -0.6 , and -0.2 V versus Ag/AgCl). (C) Extracted elemental ratio between Rb/Br and S of drop-casted 20% EG-PEDOT:PSS after first dedoping/redoping and multiple dedoping/redoping processes. (D) Cation kinetic curves during the first dedoping process of different heights, with Rb^+ in violet.

in a mixed solution of 50 mM RbBr and HBr, as well as a pure 100 mM HBr solution. The electrochromic moving front in the pure HBr solution was faster than that in the mixed solution, and both were substantially faster than the pH-neutral 100 mM RbBr electrolyte previously measured optically and with operando XRF (fig. S16, A and B). After the samples cycled in HBr underwent multiple electrochemical cycles in pure RbBr, the speed of the optical moving front slowed again (fig. S16C). The results in 20% EG-PEDOT:PSS (with Rb^+) align with a previous report, suggesting that protons exhibit higher mobility in PEDOT:PSS compared to other alkali metal cations (with Na^+ , K^+) (19). This indicates that the faster optical moving front than Rb^+ moving front in 5% EG-PEDOT:PSS is very likely due to a minority population of unexchanged protons.

To provide additional evidence for this finding, we used a cation exchange resin to replace the protons in the 5% EG-PEDOT:PSS solution with alkali metal cations. The resulting film, cast from the cation-exchanged solution, exhibited a notably slower ($\sim 2/3$) optical moving front compared to the film produced from the unexchanged solution (fig. S17).

The difference in proton transport between films cast from dispersions with 20 and 5% EG content may stem from not only a difference in residual proton concentration but also a difference in mesoscale structure. The ion composition of drop-casted 5% EG- and 20% EG-PEDOT:PSS used in electrochemical cycling was similar

(figs. S8B and S9A). Increasing the EG content can substantially enhance the phase separation of PSS-rich and PEDOT-rich domains (20). The phase boundary of 5% EG-PEDOT:PSS is not as clear as that of 20% EG-PEDOT:PSS. As mentioned in the electrochromic process, PSS-rich matrices have a low concentration of protons and are hypothetically saturated by Rb^+ . In 20% EG-PEDOT:PSS, a decrease in proton concentration leads to a diminished proton flux through the PSS-rich matrices, resulting in a reduced contribution to the overall flux driving the electrochromic front (Fig. 4C). In 5% EG-PEDOT:PSS, less clear phase boundary may lead to a better connected PEDOT network that can facilitate proton transport (Fig. 4D). Furthermore, the PEDOT-rich core in 20% EG-PEDOT:PSS is likely less hydrophilic compared to that in 5% EG-PEDOT:PSS, primarily attributable to its reduced PSS content (20). This decreased hydrophilicity in 20% EG-PEDOT:PSS results in reduced swelling of the PEDOT-rich core, akin to the previous observation of limited PEDOT crystallite lattice swelling despite the more pronounced overall swelling in PEDOT:PSS films (25). Consequently, the proton mobility within the less hydrophilic, less swollen PEDOT-rich cores is expected to decrease, as it is less conducive to the Grotthuss mechanism (34). Conversely, faster proton transport in 5% EG-PEDOT likely screens the electric field sensed by Rb^+ , making the difference between Rb^+ and proton moving fronts more pronounced.

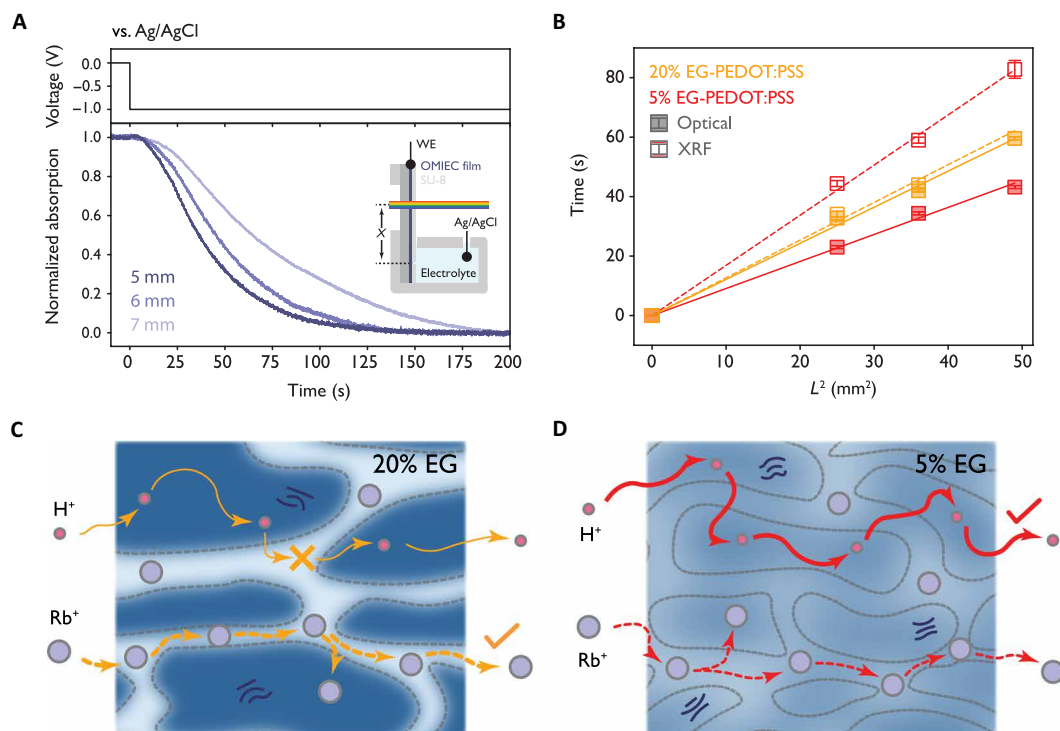


Fig. 4. The comparison between optical and XRF moving front. (A) Optical moving front in a dedoping process after multiple electrochemical cycles at different probing heights, X . **(B)** Temporal evolution of the ion drift length L in optical (solid square and line) and XRF elemental moving front (hollow square and dash line). Diagram for the Rb^+ cation (violet) and residue protons (red) transport between mesoscale domains (gray dash lines) in **(C)** 20% EG-PEDOT:PSS (orange) and **(D)** 5% EG-PEDOT:PSS (red).

These results demonstrate that operando XRF can track elemental-specific moving fronts and can distinguish ion transport behaviors among different ions within OMIECs. By combining information from optical observations, XRF data, and previous x-ray scattering research, a multimodal approach was used to better understand ion transport behaviors and accurately determine ion mobility during operation.

Thickness dependent ion mobility

To further investigate the influence of the interface on ion composition and transport, we performed operando XRF on spin-coated films with reduced thickness. The resulting XRF spectra revealed a thickness-dependent anion injection, challenging the previously reported bulk Donnan exclusion in these interface dominated systems (25). In particular, when using a thin single-layer spin-coated film (20% EG-PEDOT:PSS, ~ 100 nm), anions could enter the film under a dedoping voltage of -1 V versus Ag/AgCl. During the dedoping process, the XRF peak at 11.7 keV increased in intensity and progressively shifted to 11.9 keV (fig. S18A), indicating the presence of Br^- ions in the film (also in fig. S19). The Br and Rb compositions were deconvoluted and shown in fig. S18B. X-ray photoelectron spectroscopy (XPS) confirmed the existence of both Rb^+ and Br^- ions in the bulk, with Rb^+ ions exhibiting higher concentration at the SU-8/OMIEC interface, while Br^- ions were more concentrated at the parylene/OMIEC interface (fig. S20). In the limit of very thin films (~ 100 nm), stress concentration during initial electroswelling (OMIEC swelling with electrolyte) may introduce microscopic voids that lack fixed polyanionic charges, allowing the infiltration of liquid electrolyte, and ultimately leading to the breakdown of Donnan exclusion. Subsequent electrochemical

cycling revealed that the doping process of the material was dominated by mobile Br^- rather than Rb^+ (fig. S18C). Br^- peaks were observed in the thicker three- and five-layer spin-coated films (300 to 500 nm), but the anion concentration remained constant, indicating that anions were trapped (or not participating in the doping/dedoping) during the electrochemical cycling process (figs. S21 and S22). Thickness-dependent anion injection was also observed in 5% EG-PEDOT:PSS (figs. S23 to S26 and section S4). The thin samples that contained mobile anions demonstrated an exceptionally high ion mobility, resulting in a rapid moving front that covers a larger distance (>1.5 cm after the first applied voltage for 10 hours; fig. S27), indicating that the presence of mobile anions facilitates ion transport within the OMIEC film.

The magnitude of the interfacial contribution to overall ion transport and an estimate of bulk cation mobility in OMIECs were ascertained by studying samples of different thickness. The temporal response fit for different thicknesses of 20% EG- and 5% EG-PEDOT:PSS films was plotted in Fig. 5 (A and B, respectively), from which the mobility of cations in the film decreases with increasing film thickness. Plots of the ion mobility versus inverse sample thickness (discussion of sample thickness can be found in the Supplementary Materials) showed a linear relationship (Fig. 5C). The extrapolation of these two curves gave an estimated bulk mobility from the limit of thickness approaching infinity. Compared to 5% EG-PEDOT:PSS ($1.0 \times 10^{-3} \text{ cm}^2 \text{ s}^{-1} \text{ V}^{-1}$), 20% EG-PEDOT:PSS showed a smaller linear slope but a higher bulk cation mobility ($3.1 \times 10^{-3} \text{ cm}^2 \text{ s}^{-1} \text{ V}^{-1}$). This implied a more homogenous ion mobility distribution in 20% EG-PEDOT:PSS samples across different thickness, while the ion mobility of 5% EG-PEDOT:PSS shown more thickness dependency, apparently due to enhanced interfacial ion transport (Fig. 5D). The

interfacial transport related to a hydrophilic PSS⁻ layer has been reported (35), giving a similar estimated bulk mobility of $2 \times 10^{-3} \text{ cm}^2 \text{ s}^{-1} \text{ V}^{-1}$. These calculations yielded a much faster bulk migration rate of Rb⁺ than the electro wetting rate and represented the ion mobility in hydrated/swelled polymer. As noted above, during electrochemical cycling, a dominant majority of ions (>90%) are retained within the film, allowing cations to migrate between sites instead of traversing the entire electrochromic region from external electrolyte.

Determining the bulk mobility and isolating interfacial effects holds practical importance for different OECT architectures (and more broadly, OMIEC devices). In cOECTs, ions migrate into the film primarily via the bulk and orthogonally to the interfacial ion transport directions and thus are minimally affected by interfacial effects. However, in vOECTs, the top and bottom encapsulation of the OMIEC thin film create interfaces that are parallel to ion transport directions, and the pronounced interfacial effects accelerate ion drift diffusion. These findings have the potential to advance the optimization of OECT materials choice and fabrication schemes. For instance, implementing suitable surface treatments and decreasing the film thickness in vOECTs has the potential to further improve the device's response time.

Mobile ion density

In addition to the electrochromic moving front, we can also obtain the mobile ion density and electronic-ionic coupling efficiency through operando XRF (section S5 and Fig. 6A). On the basis of the reported model that presumes a linear electronic field decay in the dedoped region (19), the mobile cation density P can be extracted from the slope of current density j and inverse square root of time

$t^{-1/2}$. Ideally, this mobile cation density should be equal to the injected ion concentration. The linear fitting yields mobile cation density of 3.0 and $2.2 \times 10^{20} \text{ cm}^{-3}$ for drop-casted 20% EG- and 5% EG-PEDOT:PSS (gray box in Fig. 6B and thickness dependence also in fig. S28), respectively. These numbers are in line with a previous report (19) and are slightly higher than the concentration of injected Rb⁺. Taking drop-casted 20% EG-PEDOT:PSS as an example, assuming that the Rb-to-S ratio in the dedoped state is 0.7, and the modulation between the dedoped and doped states is less than 10%, we can conclude that the Rb⁺ concentration involved in the electrochemical cycling process is less than $2.6 \times 10^{20} \text{ cm}^{-3}$ (section S6; 87% of mobile cation density P). This discrepancy between the Rb⁺ concentration change and mobile cation density also results in a slightly lower than 100% electronic-ionic coupling efficiency (e.g., Faradaic side reactions consuming some electronic charge). Given an electronic charge transfer of 0.058 μmol (or $29.4 \text{ F}\cdot\text{cm}^{-3}$, from measured currents shown in fig. S29), the electronic-ionic coupling efficiency is 93% (section S6), close to the result from a previous operando NMR report (16). In summary, the combination of the measured currents and operando XRF demonstrates that Rb⁺ remains the primary cation being transported. In addition, the minor discrepancies between the XRF results and the measured currents could be attributed to proton transport or Faradaic reactions occurring at the encapsulation opening.

DISCUSSION

Ionic mean drift-diffusion length

By analyzing the measured currents in samples with different thicknesses, a relationship was established between the mobile cation density P , XRF cation mobility μ , and sample thickness d .

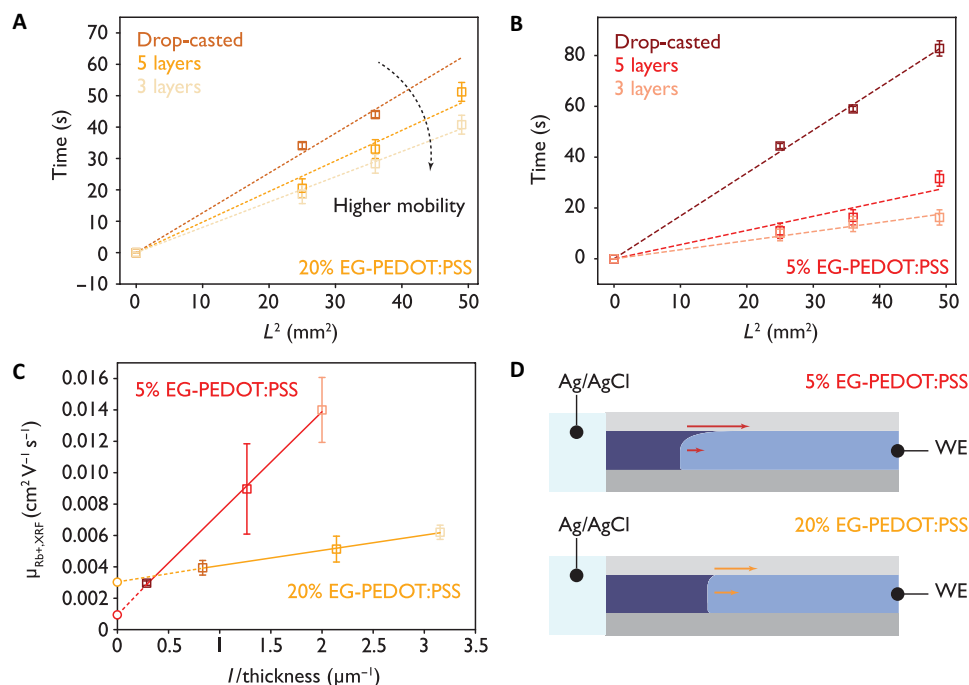


Fig. 5. Thickness-dependent ion mobility in EG-PEDOT:PSS. Temporal evolution of the ion drift-diffusion length L of Rb⁺ in (A) 20% EG-PEDOT:PSS and in (B) 5% EG-PEDOT:PSS. (C) Thickness-dependent Rb⁺ mobility in 20% EG-PEDOT:PSS (orange) and 5% EG-PEDOT:PSS (red), highlighting the bulk mobility extrapolated using colored hollow circles; (D) diagram for interface (between SU-8 encapsulation and PEDOT:PSS) and bulk ion mobility in 20% EG-PEDOT:PSS (orange) and 5% EG-PEDOT:PSS (red), highlighting how increased EG content suppresses the interfacial enhancement of ion mobility.

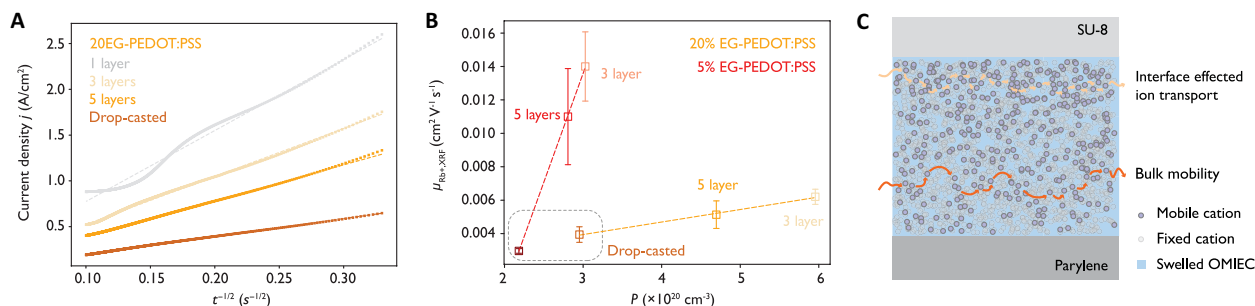


Fig. 6. The relationship between mobile ion density and ion mobility. (A) Temporal evolution of recorded current density of 20% EG-PEDOT:PSS of different thickness. (B) Rb mobility from XRF as a function of the extracted mobile cation density P ; the drop-casted samples that reflect majorly bulk mobility were highlighted with gray box. (C) Diagram for interface and bulk mobile charge density and the related ion transport pathway.

For PEDOT:PSS samples with the same EG content, the XRF-determined cation mobility μ was found to be proportional to the mobile cation density P (Fig. 6B). Given the relatively low population of protons and anions that participate in ion transport, the calculated P primarily reflects the mobile Rb^+ density in the sample. As the film thickness increased, both mobile Rb^+ density and mobility decreased notably, indicating a higher mobile cation density at the OMIEC-encapsulation interface, compared to the bulk. This result is particularly noteworthy as the migration of ions in OMIECs is relayed by the reorganization of mobile cations rather than a single cation directly migrating from external electrolyte to the optical moving front. Thus, a higher density of cations at the OMIEC-encapsulation interface implies a shorter mean drift-diffusion length for individual cations. This is analogous to shorter hops occurring at a higher rate than longer hops, leading to an accelerated migration rate of cations near the interface (Fig. 6C). This also explains the previously reported slight increase of the mobility with external salt concentration (19) and the temperature-dependent ion mobility in ionomers (36).

Mesoscale phase separation also influences the mobile cation density-mobility relationship. The slope of P - μ plot was inversely proportional to the heterogeneity of ion distribution caused by phase separation. This heterogeneity reflected the ion transport pathway distortion from ideal one-dimensional transport (section S7). In 20% EG-PEDOT:PSS, due to larger PEDOT-rich domain size and more distinct phase boundaries, the Rb^+ transport pathway was likely more tortuous compared to that of 5% EG-PEDOT:PSS. This likely led to an increased mean drift-diffusion length compared to the 5% EG-PEDOT:PSS sample with the same mobile cation density. This observation underscores the additional complexity imparted by phase separation on cation transport behavior.

Electric field-corrected ion mobility

Accurately determining the ion mobility within OMIECs also requires understanding the field distribution in the system. The presence of different ions and ion drift-diffusion behavior can potentially lead to differences in the calculated ion mobility.

In the presence of other ions, the optical moving front actually reflects the proton migration rate in 5% EG-PEDOT:PSS, which leads to a systematic error in the migration rate of Rb^+ measured by operando XRF. Because of the proton dedoping of the OMIEC, the electric field sensed by Rb^+ is smaller than that in the previously mentioned model. The time-dependent electric field in the OMIEC can be calculated through the optical moving front and thus modifying the ion migration rate model (section S5). This gives

$$\mu_{\text{Rb}^+} = \sqrt{\mu_{\text{optical}, H^+} \mu_{\text{XRF}, \text{Rb}^+}} \quad (1)$$

The proton-decoupled Rb^+ mobility in 5% EG-PEDOT:PSS (2.1 to $2.6 \times 10^{-3} \text{ cm}^2 \text{ s}^{-1} \text{ V}^{-1}$) is larger than the mobility directly calculated from XRF moving front. This result suggests a slightly lower bulk Rb^+ mobility in 5% EG-PEDOT:PSS compared to 20% EG-PEDOT:PSS. Despite this correction not altering the main conclusions, it underscores the necessity of a multimodal approach to accurately measure ion mobility within OMIECs.

A recent study introduced a quasi-field drift-diffusion model (23), revealing that hole diffusion induces a broadening of the electric field, which plays a more important role in ion transport than initially expected. The ion mobility can be calculated using an extra correction scaling parameter from the ratio of maximum moving front length L_{max}^2 and t in Fig. 5 (A and B) (detail in section S8). This result ($4.5 \times 10^{-4} \text{ cm}^2 \text{ s}^{-1} \text{ V}^{-1}$ for drop-casted 20% EG-PEDOT:PSS) suggests a lower quasi-field ion mobility than the classical ion diffusion model, leading to a cation mobility slightly lower than that in water. However, this raises questions about the applicability of the quasi-field drift-diffusion model to the specific device geometry used in operando XRF measurements, potentially due to the variable length that the moving front traverses.

Summary and outlook

We developed a new operando XRF technique to detect ion composition and mobility in bulk OMIEC thin films in real time. External salt cations migrate into the OMIEC in the first electrochemical cycle through electrowetting, followed by a weak relative modulation (5 to 10% of the cation concentration, compared to initial dedoped state) in subsequent cycles. Notably, this weak relative modulation is smaller than the systematic error in previously reported ex situ measurements ($\sim 7\%$) (25) and emphasizes the importance of operando ion composition studies. In addition, we compared the ion mobility obtained from the compositional modulation with the standard optical moving front experiment. Our findings indicate that the optical method accurately reflects ion migration rates in thick films with obvious phase separation. However, in most other cases, the assumptions underlying the optical method may lead to deviations from the actual ion mobility due to transport contributions of a minority proton population and interfacial enhancements of ion transport. This XRF method based on elemental moving fronts can be used for all polymers that exhibit ion migration regardless of color changes and is not limited to electrochromic OMIEC systems. To our knowledge, this is the first direct, noninvasive quantification of ion transport

in organic polymer materials under operando electrochemical conditions.

In the future, this setup can also be used for x-ray absorption fine structure measurements of the ion coordination environment within OMIECs and mid-infrared spectroscopy for the detection of bipolarons or other higher charged species in different charged states, as the optical path of this setup does not pass through the aqueous electrolyte. Certainly, this method is subject to some limitations. Selecting appropriate ions is crucial to prevent attenuation of the fluoresced x-ray signal, and extrapolations from Rb to other metal cations should be rigorously validated in the future. The challenge of achieving subsecond temporal resolution and submillimeter spatial resolution is amplified by the weak ion fluorescence signal. Specifically, for accumulation mode OMIECs with shorter moving fronts, better spatial resolution (i.e., smaller beam size) is necessary to map the concentration differences across smaller length scales. Using an appropriate voltage range is also important to prevent hole-limited charge transport constraints (22).

The unique insights into interfacial effects on ion transport in OMIECs are instrumental in guiding the molecular and device design. To enhance the ion transport performance and thus improve the device response speed, it is crucial to increase mobile ion density within the material. This can be achieved by increasing the ion concentration in the electrolyte or by disrupting the Donnan exclusion of the material. In particular, in vOECTs, interface engineering between OMIEC and encapsulation may be an effective route to speed up ion lateral transport, as pronounced interfacial effects demonstrate increased participation of mobile ions during electrochemical cycling. Furthermore, in the case of PEDOT:PSS, the presence of residual protons from incomplete proton-cation exchange substantially enhances ion migration speed, in particular in samples with inadequate phase separation, thereby facilitating faster ionic-electronic coupling during electrochemical cycling. The comprehensive information gleaned from this method is not readily accessible or straightforward using existing characterization techniques. This work points to the importance of compositional probes when characterizing such complex systems, especially considering the multiple charged species participating in electrostatic and electrochemical processes.

MATERIALS AND METHODS

Sample preparation and device fabrication

The EG-mixed PEDOT:PSS was prepared by mixing PEDOT:PSS dispersion (1%, Clevios PH1000, Heraeus) with EG [5, 20, and 50% (v/v)] and 0.2% (v/v) 4-dodecylbenzenesulfonic acid. The mixture was then filtered through a 0.45- μm polyethersulfone syringe filter (Whatman Uniflo) to get a homogenous dispersion. Sodium-exchanged PEDOT:PSSNa was synthesized via ion exchange with Amberlite IR120 Na^+ form cation exchange resin (Sigma-Aldrich). PEDOT:PSS (20 ml) was loaded onto a column packed with resin (2 g); the dispersion was passed through the resin bed under pressure for 30 min. PEDOT:PSSNa was subsequently used without further treatment.

To fabricate the device for operando XRF characterization, the glass slide was first coated with 2- μm parylene C, and ultraviolet (UV)-ozone for 30 min. The mixture was then cast on the parylene-coated glass. For each layer in the spin-coated samples, the mixtures were spun at 1000 rpm for 1 min, following a 2-min soft bake at 80°C. For the drop-casted samples, the glass was tilted on a small block. The mixtures were then dropped from the higher end of the glass to flow through the whole surface. The slide was then put on a hot

plate horizontally to achieve homogeneous surface coverage. The drop-casted sample was then dry at 80°C. The dry spin-coated and drop-casted samples were all hard baked at 140°C for 30 min, and then immersed in the deionized water to remove the residue small molecules. A 2.5- μm AZ nLOF photoresist or 25- μm SU-8 photoresist with small opening were patterned through photolithography and used as encapsulation layer. The samples were lastly hard baked at 140°C for 30 min again to remove the possible cracks on the encapsulation layer.

Operando XRF cell description

The XRF cell was 3D-printed and assembled with an Ag/AgCl counter electrode and a PEDOT:PSS-coated glass slide (Fig. 1A). The glass slide was fixed on the cell to avoid small displacement during the long-time operando XRF measurements. To prevent any external pressure that might influence the ion mobility within the OMIEC films (37), the electrolyte chamber was left unsealed, and extra electrolyte was introduced by a syringe pump to compensate the evaporation effect thus maintaining the water level. In addition, the upper surface of the cell was covered with lead tape to block the ion signal from the electrolyte.

Because of the sulfur peak attenuation in the encapsulation layer, the accurate determination of ionic composition and mobility in OMIECs requires different encapsulation thickness. A thin encapsulation layer (2.5 μm) minimized the attenuation of sulfur peaks and thus offered a high-fidelity signal for ion composition measurement. However, the thin encapsulation layer under the electrolyte level proved to be susceptible to deformation over electrochemical cycles due to the film swelling fluctuations. Consequently, this led to inaccuracies in determining ion mobility. To address the aforementioned issues, samples were prepared with a 25- μm SU-8 encapsulation layer to precisely measure the ion mobility. This thicker encapsulation layer ensured a stable and intimate contact with the OMIEC sample during multiple electrochemical cycling, enabling precise control over the ion migration distance (between the opening gap and the x-ray footprint). As a result, it facilitated a more reliable and consistent determination of ion mobility through a time-resolved electrochromic moving front.

Operando XRF and optical measurement

Operando XRF measurements were conducted in fluorescence mode using spectroscopy-grade ionization chambers (FMB Oxford). The x-ray beam size on the sample was 1.0 \times 8.0 (vertical \times horizontal) mm. Spectra were collected with excitation energies before (15,000 eV) and after (15,250 eV) the Rb K-edge to deconvolute the overlapping Br K_β and Rb K_α peaks. The cell height was controlled by a vertical direction motor, while the other motors remained fixed throughout the entire measurement. The XRF detector (silicon drift detector) was placed 65 to 70 mm away from the sample surface to maximize the sulfur (S) signal. The intensity of the incident x-ray was calibrated using the As K_α peak from the glass background, and all other peaks were normalized accordingly.

The potential control during the operando measurement was carried out using a potentiostat (Ivium) with a Ag/AgCl electrode as the reference electrode (CE/RE). To prepare the samples for the kinetic measurements, they were first dedoped at -1 V versus Ag/AgCl for 12 hours, followed by a 100-min redoping step at 0 V versus Ag/AgCl. To ensure stabilized ion transport, all samples for kinetic measurements were precycled between -1 and 0 V versus Ag/AgCl for at least five cycles.

For 5% EG- and 20% EG-drop-casted samples, optical moving front was recorded immediately after the XRF measurement using a spatially resolved camera. The optical moving front for the remaining samples was measured on the benchtop using the same method. Data analysis was performed using Python scripts and ImageJ software.

UV-vis spectroscopy

To prepare UV-visible (UV-vis) spectroscopy samples, 20% EG-PEDOT:PSS was drop-casted on pieces of 1 cm × 2 cm parylene-coated glass cleaned with UV-ozone exposure. The SU-8 encapsulation layer was prepared as the operando XRF samples. The beam height relative to the opening was tuned by adjusting the poly(methyl methacrylate) cuvette height, and the beam size was determined as 2 mm. The UV-vis spectroscopy was collected in 100 mM aqueous RbBr with an Ag/AgCl pellet (Warner Instruments) reference/counter electrode. Potential control and current measurement were carried out with a potentiostat (Ivium). Simultaneous absorption spectroscopy was recorded with a halogen white light source (Ocean Optics, DH-2000-BAL) and an optical fiber to UV-vis (Ocean Optics, FLAME-S) spectrometers with 200-ms integration times. Electrochemical and spectroscopic data were recorded with Iviumsoft and OceanView software, respectively. Data analysis was performed using Python scripts.

Ex situ XPS measurement and depth profile

The XPS spectra were taken using a Thermo Fisher Scientific ESCALAB 250Xi equipped with a monochromatic KR Al x-ray source (spot size of 500 μm) at the Northwestern University Atomic and Nanoscale Characterization Experimental Center (NUANCE). Before data collection, a flood gun was used for charge compensation. The S peak was measured without ionic etching to avoid the reduction of sulfonate. For depth profile, the sample was peeled from the substrate and transferred onto a silicon wafer (fig. S20B). The ionic beam (area, 3 mm × 3 mm) etching time for each data point was set at 30 s (~10 nm). The curve fitting was performed with Avantage (Thermo Fisher Scientific) software.

Supplementary Materials

This PDF file includes:

Supplementary Text
Figs. S1 to S30
Tables S1 and S2

REFERENCES AND NOTES

- B. D. Paulsen, K. Tybrandt, E. Stavrinidou, J. Rivnay, Organic mixed ionic-electronic conductors. *Nat. Mater.* **19**, 13–26 (2020).
- D. Moia, A. Giovannitti, A. A. Szumska, I. P. Maria, E. Rezasoltani, M. Sachs, M. Schnurr, P. R. F. Barnes, I. McCulloch, J. Nelson, Design and evaluation of conjugated polymers with polar side chains as electrode materials for electrochemical energy storage in aqueous electrolytes. *Energ. Environ. Sci.* **12**, 1349–1357 (2019).
- X. D. Ji, B. D. Paulsen, G. K. K. Chik, R. H. Wu, Y. Y. Yin, P. K. L. Chan, J. Rivnay, Mimicking associative learning using an ion-trapping non-volatile synaptic organic electrochemical transistor. *Nat. Commun.* **12**, 2480 (2021).
- P. C. Harikesh, C. Y. Yang, D. Y. Tu, J. Y. Gerasimov, A. M. Dar, A. Armada-Moreira, M. Massetti, R. Kroon, D. Bliman, R. Olsson, E. Stavrinidou, M. Berggren, S. Fabiano, Organic electrochemical neurons and synapses with ion mediated spiking. *Nat. Commun.* **13**, 901 (2022).
- R. B. Rashid, X. D. Ji, J. Rivnay, Organic electrochemical transistors in bioelectronic circuits. *Biosens. Bioelectron.* **190**, 113461 (2021).
- C. Pitsalidis, A. M. Pappa, A. J. Boys, Y. Fu, C. M. Moysidou, D. van Niekerk, J. Saez, A. Savva, D. Iandolo, R. M. Owens, Organic bioelectronics for in vitro systems. *Chem. Rev.* **122**, 4700–4790 (2022).
- G. Dufil, I. Bernacka-Wojcik, A. Armada-Moreira, E. Stavrinidou, Plant bioelectronics and biohybrids: The growing contribution of organic electronic and carbon-based materials. *Chem. Rev.* **122**, 4847–4883 (2022).
- X. Ji, X. Lin, J. Rivnay, Organic electrochemical transistors as on-site signal amplifiers for electrochemical aptamer-based sensing. *Nat. Commun.* **14**, 1665 (2023).
- R. B. Rashid, W. Y. Du, S. Griggs, I. P. Maria, I. McCulloch, J. Rivnay, Ambipolar inverters based on cofacial vertical organic electrochemical transistor pairs for biosignal amplification. *Sci. Adv.* **7**, eabh1055 (2021).
- J. Rivnay, S. Inal, A. Salleo, R. M. Owens, M. Berggren, G. G. Malliaras, Organic electrochemical transistors. *Nat. Rev. Mater.* **3**, 17086 (2018).
- J. Tropp, D. Meli, J. Rivnay, Organic mixed conductors for electrochemical transistors. *Matter* **6**, 3132–3164 (2023).
- G. Garcia-Belmonte, J. Bisquert, G. S. Popkirov, Determination of the electronic conductivity of poly(bithiophene) films at different doping levels using in situ electrochemical impedance measurements. *Appl. Phys. Lett.* **83**, 2178–2180 (2003).
- D. A. Bernards, G. G. Malliaras, Steady-state and transient behavior of organic electrochemical transistors. *Adv. Funct. Mater.* **17**, 3538–3544 (2007).
- A. Savva, S. Wustoni, S. Inal, Ionic-to-electronic coupling efficiency in PEDOT:PSS films operated in aqueous electrolytes. *J. Mater. Chem. C* **6**, 12023–12030 (2018).
- A. Savva, C. Cendra, A. Giugni, B. Torre, J. Surgailis, D. Ohayon, A. Giovannitti, I. McCulloch, E. Di Fabrizio, A. Salleo, J. Rivnay, S. Inal, Influence of water on the performance of organic electrochemical transistors. *Chem. Mater.* **31**, 927–937 (2019).
- D. Lyu, Y. Jin, P. C. M. Magusin, S. Sturmiolo, E. W. Zhao, S. Yamamoto, S. T. Keene, G. G. Malliaras, C. P. Grey, Operando NMR electrochemical gating studies of ion dynamics in PEDOT:PSS. *Nat. Mater.* **22**, 746–753 (2023).
- S. Warren, G. Munteanu, D. Rathod, T. McCormac, E. Dempsey, Scanning electrochemical microscopy imaging of poly(3,4-ethylenedioxythiophene)/thionine electrodes for lactate detection via NADH electrocatalysis. *Biosens. Bioelectron.* **137**, 15–24 (2019).
- R. Giridharagopal, L. Q. Flagg, J. S. Harrison, M. E. Ziffer, J. Onorato, C. K. Luscombe, D. S. Ginger, Electrochemical strain microscopy probes morphology-induced variations in ion uptake and performance in organic electrochemical transistors. *Nat. Mater.* **16**, 737–742 (2017).
- E. Stavrinidou, P. Leleux, H. Rajaona, D. Khodagholy, J. Rivnay, M. Lindau, S. Sanaur, G. G. Malliaras, Direct measurement of ion mobility in a conducting polymer. *Adv. Mater.* **25**, 4488–4493 (2013).
- J. Rivnay, S. Inal, B. A. Collins, M. Sessolo, E. Stavrinidou, X. Strakosas, C. Tassone, D. M. Delongchamp, G. G. Malliaras, Structural control of mixed ionic and electronic transport in conducting polymers. *Nat. Commun.* **7**, 11287 (2016).
- S. Inal, G. G. Malliaras, J. Rivnay, Optical study of electrochromic moving fronts for the investigation of ion transport in conducting polymers. *J. Mater. Chem. C* **4**, 3942–3947 (2016).
- S. T. Keene, J. E. M. Laulainen, R. Pandya, M. Moser, C. Schnedermann, P. A. Midgley, I. McCulloch, A. K. Rao, G. G. Malliaras, Hole-limited electrochemical doping in conjugated polymers. *Nat. Mater.* **22**, 1121–1127 (2023).
- S. T. Keene, A. Rao, G. G. Malliaras, The relationship between ionic-electronic coupling and transport in organic mixed conductors. *Sci. Adv.* **9**, eadi3536 (2023).
- W. Huang, J. H. Chen, Y. Yao, D. Zheng, X. D. Ji, L. W. Feng, D. Moore, N. R. Glavin, M. Xie, Y. Chen, R. M. Pankow, A. Surendran, Z. Wang, Y. Xia, L. B. Bai, J. Rivnay, J. F. Ping, X. G. Guo, Y. H. Cheng, T. J. Marks, A. Facchetti, Vertical organic electrochemical transistors for complementary circuits. *Nature* **613**, 496–502 (2023).
- R. Wu, B. D. Paulsen, Q. Ma, I. McCulloch, J. Rivnay, Quantitative composition and mesoscale ion distribution in p-type organic mixed ionic-electronic conductors. *ACS Appl. Mater. Interfaces* **15**, 30553–30566 (2023).
- B. Y. Ouyang, C. W. Chi, F. C. Chen, Q. F. Xi, Y. Yang, High-conductivity poly(3,4-ethylenedioxythiophene):poly(styrene sulfonate) film and its application in polymer optoelectronic devices. *Adv. Funct. Mater.* **15**, 203–208 (2005).
- C. M. Palumbino, C. Heller, C. J. Schaffer, V. Korstgens, G. Santoro, S. V. Roth, P. Muller-Buschbaum, Molecular reorientation and structural changes in cosolvent-treated highly conductive PEDOT:PSS electrodes for flexible indium tin oxide-free organic electronics. *J. Phys. Chem. C* **118**, 13598–13606 (2014).
- J. Huang, P. F. Miller, J. S. Wilson, A. J. De Mello, J. C. De Mello, D. D. C. Bradley, Investigation of the effects of doping and post-deposition treatments on the conductivity, morphology, and work function of poly(3,4-ethylenedioxythiophene)/poly(styrene sulfonate) films. *Adv. Funct. Mater.* **15**, 290–296 (2005).
- R. H. Wu, B. D. Paulsen, Q. Ma, J. Rivnay, Mass and charge transport kinetics in an organic mixed ionic-electronic conductor. *Chem. Mater.* **34**, 9699–9710 (2022).
- S. Zhang, P. Kumar, A. S. Nouas, L. Fontaine, H. Tang, F. Cicaira, Solvent-induced changes in PEDOT:PSS films for organic electrochemical transistors. *Appl. Mater.* **3**, 014911 (2015).
- L. Q. Chen, E. Bonaccorso, Electrowetting – From statics to dynamics. *Adv. Colloid Interface Sci.* **210**, 2–12 (2014).
- G. D. Spyropoulos, J. N. Gelinis, D. Khodagholy, Internal ion-gated organic electrochemical transistor: A building block for integrated bioelectronics. *Sci. Adv.* **5**, eaau7378 (2019).

33. T. J. Quill, G. LeCroy, D. M. Halat, R. Sheelamantula, A. Marks, L. S. Grundy, I. McCulloch, J. A. Reimer, N. P. Balsara, A. Giovannitti, A. Salleo, C. J. Takacs, An ordered, self-assembled nanocomposite with efficient electronic and ionic transport. *Nat. Mater.* **22**, 362–368 (2023).
34. N. Amdursky, E. D. Glowacki, P. Meredith, Macroscale biomolecular electronics and ionics. *Adv. Mater.* **31**, e1802221 (2019).
35. T. Khan, T. McAfee, T. Ferron, A. Alotaibi, B. Collins, Local chemical enhancement and gating of organic coordinated ionic-electronic transport. (2022).
36. D. Fragiadakis, S. C. Dou, R. H. Colby, J. Runt, Molecular mobility, ion mobility, and mobile ion concentration in poly(ethylene oxide)-based polyurethane ionomers. *Macromolecules* **41**, 5723–5728 (2008).
37. X. K. Wang, X. F. Li, J. G. Mei, K. J. Zhao, Doping kinetics in organic mixed ionic-electronic conductors: Moving front experiments and the stress effect. *Extreme Mech. Lett.* **54**, 101739 (2022).

Acknowledgments: We thank Z. Laswick for the discussions. **Funding:** R.W., B.D.P., and J.R. acknowledge funding from the NSF (grant no. NSF DMR-1751308). This work was also supported by funding from the Northwestern Materials Research Science and Engineering Center (NSF DMR-2308691). J.T. was primarily supported by an Office of Naval Research (ONR) Young Investigator Program (YIP) award no. N00014-20-1-2777. The synchrotron XRF work was performed at the 5-BM-D beamline of the DuPont-Northwestern-Dow Collaborative Access

Team (DND-CAT), located at Sector 5 of the Advanced Photon Source (APS). DND-CAT is supported by Northwestern University, The Dow Chemical Company, and DuPont de Nemours Inc. Facility operated for the DOE Office of Science by Argonne National Laboratory under contract no. DE-AC02-06CH11357. This work made use of the NUFAB, IMSERC, and NUANCE facility of Northwestern University, which has received support from the Shyne Resource (NSF ECCS-2025633), the NU's Materials Research Science and Engineering Center (NSF DMR-2308691), the IIN. **Author contributions:** Conceptualization: R.W., X.J., B.D.P., and J.R. Methodology: R.W., X.J., Q.M., and J.T. Resource: R.W., X.J., and J.T. Investigation: R.W., X.J., and Q.M. Formal analysis: R.W. and X.J. Visualization: R.W. and X.J. Supervision: J.R., X.J., and R.W. Writing—original draft: R.W., X.J., and J.R. Writing—review and editing: R.W., X.J., B.D.P., J.T., and J.R. **Competing interests:** The authors declare that they have no competing interests. **Data and materials availability:** All data needed to evaluate the conclusions in the paper are present in the paper and/or the Supplementary Materials. The original XRF and UV-vis data underlying the figures in the main text are publicly available from the Northwestern University repository (Dryad) at <https://doi.org/10.5061/dryad.jdfn2z3j9>. The Python codes for data analysis are publicly available at <https://doi.org/10.5281/zenodo.10823319>.

Submitted 4 January 2024

Accepted 19 March 2024

Published 24 April 2024

10.1126/sciadv.adn8628